



Article

The Effect of Heat Treatment on the Microstructure and Mechanical Properties of Plasma-Cladded CoCrFeNiMn Coatings on Compacted Graphite Iron

Bo Zhang ¹, Ruitao Fu ¹, Peihu Gao ^{1,2,*} , Baiyang Chen ¹, Anton Naumov ³ , Fei Li ¹, Daming Zhao ¹, Zhong Yang ^{1,2}, Yongchun Guo ^{1,2}, Jianping Li ^{1,2,*}, Lei Cheng ⁴, Jinyuan Gong ⁴, Jiawei Liu ⁴ and Yu Li ⁴

¹ School of Materials and Chemical Engineering, Xi'an Technological University, Xi'an 710021, China; 13935225325@139.com (B.Z.); ruitaofu@163.com (R.F.); baiyang2578@163.com (B.C.); lifei814990635@163.com (F.L.); zhaodaming@xacmkj.com (D.Z.); yz750925@163.com (Z.Y.); yc_guo@163.com (Y.G.)

² Shaanxi Province Engineering Research Centre of Aluminum/Magnesium Light Alloy and Composites, Xi'an 710021, China

³ Lightweight Materials and Structures Laboratory, Institute of Mechanical Engineering, Materials and Transport, Peter the Great St. Petersburg Polytechnic University, St. Petersburg 195251, Russia; anton.naumov@spbstu.ru

⁴ Shaanxi North Dynamic Co., Ltd., Baoji 721300, China; clhshm@163.com (L.C.); 18729733287@163.com (J.G.); 18700731849@163.com (J.L.); liyu@163.com (Y.L.)

* Correspondence: tigergaopei@163.com (P.G.); ljp_0103xatu@163.com (J.L.); Tel.: +86-29-83208080 (P.G.); +86-29-86173224 (J.L.)

Abstract: CoCrFeNiMn high-entropy alloy coatings were deposited on compacted graphite iron (CGI) by plasma transfer arc cladding to strengthen and improve the wear resistance (performance) of the surface. The effects of different heat treatment processes on the microstructure and mechanical properties of the CoCrFeNiMn coatings were investigated. Compared with the deposited coating, the single FCC phase in the heat-treated coatings was retained, the grain size of the columnar dendrites decreased, the spacing between the dendrites increased, and the Cr-rich precipitated phase in the grain boundary increased. The heat treatment process had a positive influence on the microhardness and wear resistance of the coatings. The microhardness of the coatings increased after heat treatment. After heat treatment at 660 °C for 90 min, the coating had the highest microhardness of $563 \pm 6.9 \text{ HV}_{0.2}$, and it had the best wear resistance.

Keywords: high entropy alloy; coating; heat treatment; microstructure; mechanical property



Citation: Zhang, B.; Fu, R.; Gao, P.; Chen, B.; Naumov, A.; Li, F.; Zhao, D.; Yang, Z.; Guo, Y.; Li, J.; et al. The Effect of Heat Treatment on the Microstructure and Mechanical Properties of Plasma-Cladded CoCrFeNiMn Coatings on Compacted Graphite Iron. *Coatings* **2024**, *14*, 374. <https://doi.org/10.3390/coatings14040374>

Academic Editor: Angela De Bonis

Received: 22 February 2024

Revised: 14 March 2024

Accepted: 20 March 2024

Published: 22 March 2024



Copyright: © 2024 by the authors. Licensee MDPI, Basel, Switzerland. This article is an open access article distributed under the terms and conditions of the Creative Commons Attribution (CC BY) license (<https://creativecommons.org/licenses/by/4.0/>).

1. Introduction

In 2004, after continuous experiments and analysis by Taiwanese scholar Ye, it was projected that five or more primary alloy elements might be additional to material at an equivalent dose, and such materials were known as “multi-principal high-entropy alloys (HEAs)” [1–4]. This splits the standard idea and suggests that the high entropy impact of multiprincipal alloys does not solely result in the microstructures of intermediate phases within the material that have an effect on the alloy’s properties. However, additionally, it ends up in the formation of solid solutions within the material’s microstructure, with high stability in their totally different cuboidal or hexagonal structures. Compared to traditional alloys, entropic alloys have excellent properties like extremely high strength [5,6], great ductility [7], good catalytic qualities [8], strong resistance to irradiation [9], high corrosion resistance [10], and outstanding resistance to wear [11]. In recent years, the research achievements of high entropy alloys have made rapid progress, and amorphous materials and composite materials are known as the three most promising materials of the twenty-first century.

The distinctive characteristics of HEAs provide outstanding performances; however, they are pricey. Therefore, from the perspective of improving performance and reducing costs, HEA coatings with superior performances on the surface of affordable base materials to enhance the surface performance of materials are proposed. The HEA coatings were deposited on the surface of the metal workpiece to be repaired or modified, which can greatly improve the mechanical properties of the surface of the metal workpiece, such as microhardness, tensile strength, corrosion resistance, and wear resistance [12]. Currently, surface modification and repair technology represent the most popular preparation process for high-entropy alloy coatings. It can be categorized into laser cladding technology [13,14], plasma cladding [15,16], thermal spraying [17], cold spraying [18], electron-beam sputtering technology [19], electrochemical deposition technology [20], etc. Compared to the commonly used methods, plasma cladding technology has the following advantage characteristics, including a high powder deposition rate, low dilution rate, high cladding efficiency, a wide selection of cladding materials, and sensible method controllability so it was preferred to prepare HEA coatings.

CoCrFeNiMn is an important new HEA material that features a uniaxially face-centered cubic (FCC) structure with high strength, good plasticity, ductility, and fracture toughness, so it has excellent potential for engineering applications. During the preparation of the coating by plasma transfer arc cladding, the quick heating and cooling characteristics of the alloy cause the elements to solidify before they can diffuse, leading to a lot of segregation and internal stress concentration that affects the coating's properties. Heat treatment of metal workpieces can achieve the purpose of eliminating defects generated during the preparation process, refining grain size, eliminating segregation, reducing welding residual stress, and homogenizing the microstructure and properties of the alloy [21,22]. Sha et al. [23] found that laser-coated AlCoCrFeNiTi_{0.5} formed a homogeneous and fine composition during heat treatment at 900 °C and annealed for 5 h. The hardened coatings showed an improvement of microhardness of about 73.5% compared to the as-deposited coatings, and the hardened coatings showed a 92.5% lower wear weight loss and a 50% reduction in wear track width compared to the as-deposited coatings. Hao et al. [24] found that the mechanical properties of the coating surface and the bond strength of the coating were improved by tempering NiCoCrAlYTa prepared by the high-velocity oxygen-fuel (HVOF) spraying technique. Lin et al. [25] prepared FeCoCrNiAl coatings using a supersonic atmospheric plasma spraying technique. Then, vacuum heat treatment was carried out at 600 °C and 900 °C. They found that the microstructure of the coatings was refined after heat treatment, and the grain refinement helped to improve the hardness and wear resistance of the coatings. Munitz et al. [26] subjected heat treatment of the AlCoCrFeNi alloy at 650–975 °C, and the phase with BCC structure between the dendrites of the alloy transformed into a tough and brittle σ phase, resulting in an improvement in the microhardness of the alloy. At 1100 °C, the σ phase remodeled into a phase with BCC structure and led to the softening of the alloy. Li et al. [27] treated the AlCrFeNi₂Ti_{0.5} alloy and found that the tensile strength of the alloy was augmented to 600 MPa, malleability was improved, and elongation was double that of the as-cast alloy below the result of precipitated particles and solid solution strengthening phases, achieving a joint improvement in strength and malleability of the high-entropy alloy. He et al. [28] found that the strength of CoCrFeNiNb_{0.25} alloy was considerably improved once the alloy was heat treated at 750 °C, whereas the compressive physical property was barely affected. Zhang et al. [29] investigated the microstructural changes, phase stability, and properties of CoCrMoNbTi_{0.4} alloy at completely different annealing temperatures. The properties of the alloy were considerably reinforced after heat treatment. Especially, the microhardness and compressive strength of the alloy reached 959 ± 2 HV_{0.5} and 1790 MPa, separately, at an associate hardening temperature of 1200 °C due to an increase in the proportion occupied by the diffusely distributed secondary phase. Zhang et al. [30] investigated the changes in properties of Al_{0.5}CoCrFeNiSi_{0.2} alloy subjected to an aging treatment at 700–1100 °C. It was found that at aging temperatures below 1000 °C, the σ -phase precipitated between the dendrites, inflicting the alloy to exhibit

important hardening and lower tensile strain. In contrast, at higher than 1000 °C, the aging temperature made a higher tensile strain than the as-cast one because of the disappearance of the dendrites and the coarsening of the microstructure. Niu et al. [31] found that the tensile properties and strength of Al_{0.5}CoCrFeNi alloy were significantly improved by the increased duration of heat treatment, and the alloy exhibited glorious tensile properties.

Most of the studies done by previous scholars mainly focused on the effects of the cladding process parameters on the microstructure and properties of the coatings, but minor attention was paid to the effect of heat treatment (e.g., temperature and holding time) on the grain size and properties of the coatings after plasma cladding. In previous work, CoCrFeNiMn coating was prepared on a cast iron substrate using PTA technology to improve the properties of the substrate, and the effects of plasma cladding current on the microstructure and the friction and wear properties of the CoCrFeNiMn coatings were mainly investigated [32].

The influence of heat treatment on the microstructure and wear performance of the CoCrFeNiMn HEA coatings seems unclear. There are few reports on the effect of heat treatment on plasma-cladded CoCrFeNiMn HEA coating. In order to improve the performance of the claddings, it is necessary to investigate the influence of heat treatment on its performance. On the basis of the previous research results [32], the coating prepared with a 65 A current was selected for this work. Thermal analysis of the coatings was carried out to develop the appropriate heat treatment process. The effects of the heat treatment temperature and holding time on the microstructure, phase composition, microhardness, friction, and wear properties of the cladded CoCrFeNiMn HEA coatings were investigated.

2. Materials and Methods

2.1. Preparation of the HEA Coatings

The alloy powder chosen for this work is an equal atomic ratio CoCrFeNiMn powder (Beijing Avemite Powder Metallurgy Technology Co., Ltd., Beijing, China), which was spherical in shape with particle size ranging from 15 to 53 μm, as shown in Figure 1. The chemical compositions of the powders are summarized in Table 1. The powders had been used in the previous work [32]. The X-ray diffraction pattern of the powder is shown in Figure 2, which shows that the powder has a single FCC phase structure. The powder was fabricated on the surface of cast iron with a size of 100 × 100 × 10 mm using a plasma welder model DML-V03BD manufactured by Shanghai Dom Machinery Co., Ltd., Shanghai, China. Figure 2 shows the X-ray diffraction pattern of the CoCrFeNiMn powder, which has a single FCC phase structure. The CGI consisted mainly of worm-like graphite as well as ferrite, as shown in Figure 3. Table 2 shows the chemical composition of the CGI. The CGI substrate has been used in other work [32]. The CGI substrates were cleaned with acetone and dried in an oven. Meanwhile, the CoCrFeNiMn powder was dried at 150 °C for 30 min before depositing. Based on the previous work [32], the following plasma deposition parameters were chosen for this work: the distance between the plasma torch and the substrate was kept at 10 mm, and the scanning speed was 180 mm/min. The ion gas flow rate and protective gas flow rate were 2.0 L/min and 8.0 L/min, respectively. The powder feed rate was maintained at 10 r/min. The overlap width of the multilayer cladding was 4 mm. The plasma arc current was 65 A.

Table 1. Elemental composition of CoCrFeNiMn powder [32].

| Elements | Co | Cr | Fe | Ni | Mn |
|-------------|-------|-------|-------|-------|-------|
| Content/wt% | 20.58 | 18.35 | 19.98 | 20.49 | 20.48 |

Table 2. Chemical composition of the CGI substrate [32].

| Elements | C | Si | Mn | S | P | Fe |
|-------------|---------|---------|------|------|-------|-----|
| Content/wt% | 3.4–3.7 | 2.4–3.0 | ≤0.6 | ≤0.6 | ≤0.06 | Bal |

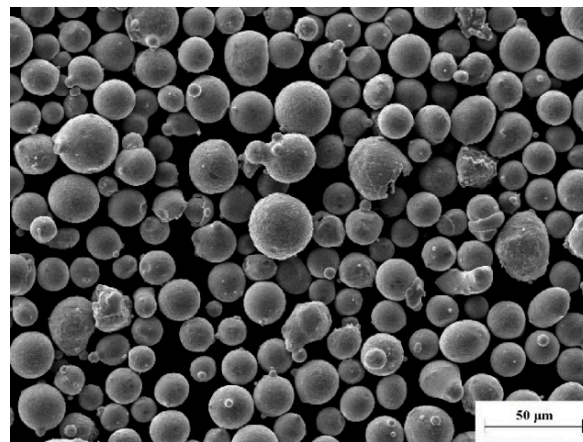


Figure 1. Microstructure of CoCrFeNiMn powder [32].

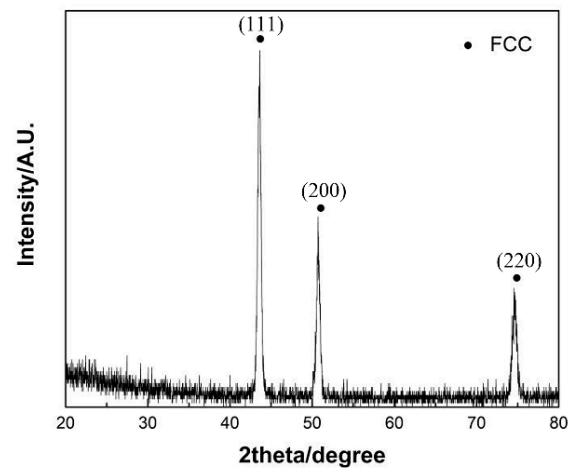


Figure 2. XRD pattern of the CoCrFeNiMn powder [32].

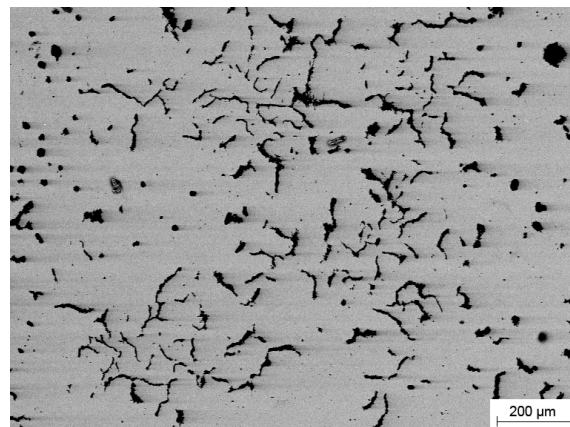


Figure 3. Microstructure of the CGI substrate [32].

2.2. Heat Treatment Processes

The CoCrFeNiMn coatings and substrate were cut into block specimens through wire-cut machining (WEDM). The free-stand coating was analyzed through STA 449C (NETZSCH GABO Instruments GmbH, Selb, Germany) with a sample weight of 10 mg and a breadth of over 5 mm, heated up to 1200 °C at a rate of 10 °C per min. The DSC results of the coating are shown in Figure 4. The preferred heat treatment temperature and time were selected according to the DSC characteristic peaks. The heat treatment

processing parameters are listed in Table 3. The block specimens were heat treated in an atmosphere protection furnace (KSL-1100X, Hefei Kejing Instrument Co., Ltd., Hefei, China) with argon as a protection gas. The phases and microhardness of the heat-treated coatings were analyzed. The impact of heat treatment on the microstructure, strength, and wear resistance of the coating was investigated.

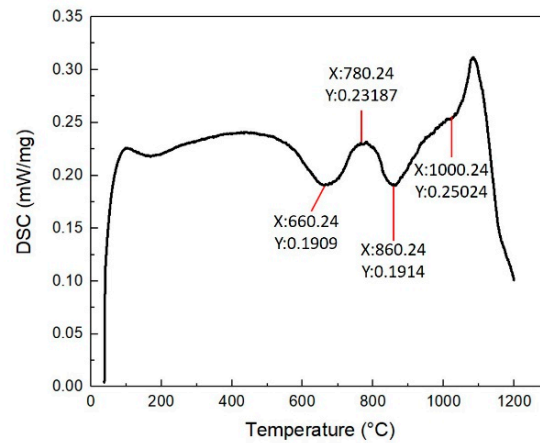


Figure 4. DSC curves of plasma-cladded CoCrFeNiMn coatings.

Table 3. Heat treatment processing.

| Temperature/°C | | Time/min | |
|----------------|----|----------|----|
| 660 | 30 | 60 | 90 |
| 780 | 30 | 60 | 90 |
| 860 | 30 | 60 | 90 |
| 1000 | 30 | 60 | 90 |

2.3. Characterization of the HEA Coatings

The microstructures of the powders and coatings were characterized by scanning electron microscopy (SEM, VEGA II-XMU, TESCAN, Bron, Czech Republic), and the elements of the coatings were characterized by EDS. The samples were etched with a 10% alcoholic solution of nitric acid for 3 s. The physical phases of the powders and coatings were analyzed by an X-ray diffractometer (D2, Bruker, Billerica, MA, USA) using Cu K α radiation. The microhardness of the coatings was tested by a Vickers tester (HV-5, Shanghai Taimin, Shanghai, China) with a test load of 200 gf and a test time of 30 s at intervals of 200 μ m from the top of the coatings to the heat-affected zone, as shown in Figure 5. To ensure data accuracy, the microhardness test was repeated three times for each sample to increase accuracy.

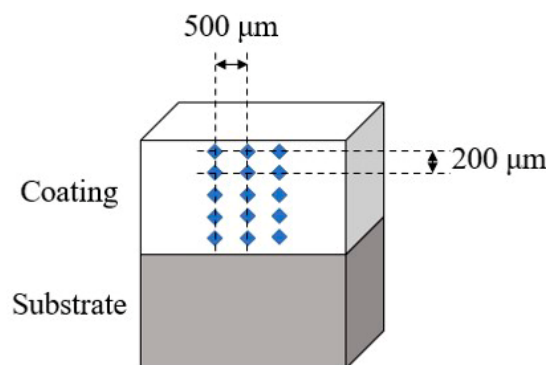


Figure 5. Diagram of microhardness test.

2.4. Wear Test

Figure 6 shows the diagram of the wear test. The specimens were cut using wire cutting into cylindrical friction wear test specimens with a size $\varphi 30 \times 5$ mm, where the coating thickness was 3 mm, the substrate thickness was 2 mm, and they were heat treated. For wear tests in a dry friction environment, the wear test was carried out with the pin kept fixed at 6 mm from the center of the plate and the plate rotated around its axis. The friction and wear test was carried out at 25 °C with a load of 10 N, a speed of 300 rad/min, and a test time of 30 min using an HT1000 friction and wear tester manufactured by Lanzhou Zhongke Kaihua Technology Development Co., Ltd., Beijing, China. In the friction and wear test, an N80 (nickel-based alloy, type N80, the same material as used in a valve part assembled in the compacted cast iron cylinder head, microhardness: 526–545 HV) pin with the size of $\varphi 3 \times 10$ mm was selected as the counterpart for coating. The wear mass loss of the coating was measured by weighing the samples before and after the wear test by using an electronic balance. After the wear test, the wear morphology was characterized by SEM and 3D confocal microscopy (VK-X3000, Keyence, Osaka, Japan).

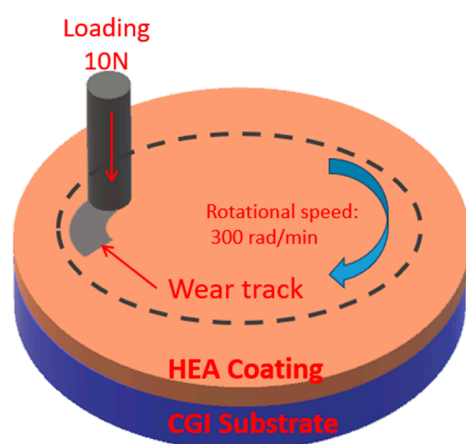


Figure 6. Diagram of wear test.

3. Results and Discussion

3.1. Microstructure

Figure 7 shows the cross-sectional microstructure of the as-cladded and heat-treated ones in the middle part of the coating. The microstructure of the as-cladded coating mainly consists of columnar and equiaxed grains related to the heat flow in the molten pool during the multipass cladding process as well as the cyclic heating and cooling in the overlapped region. According to the theory of solidification thermodynamics and the direction of heat dissipation, fine equiaxed grains were generated in the top and bottom regions of the as-cladded coating because the cooling rate in these regions was greater than that in the middle of the coating, and the rate of grain growth was much lower than the growth rate. For the middle part of the as-cladded coating, the cooling rate of the liquid metal was slower, which was favorable for grain growth but not for grain nucleation, so the grain shape in the middle part of the coating was mainly coarse columnar digital grains, as shown in Figure 7. According to the thermodynamic theory of solidification and the direction of heat dissipation, i.e., the rate of nucleation and growth of grains depends mainly on the crystallization parameter G/R (G is the temperature gradient and R is the solidification rate) [12]. Due to the large temperature gradient at the top and bottom of the coating and the high solidification rate, fine equiaxed grains were generated in the top and bottom regions of the cladding coating. As shown in Figure 7b, it was the transition zone of the cladding layer. At a large degree of supercooling, the transition zone forms a structure dominated by Letenite, as discussed in previous work [32]. As the heat treatment temperature increased, the amounts of columnar grain within the middle of the coating decreased, the quantity of equiaxed grain increased, the interdendritic region coarsened step by step, and solid

solutions precipitated at the interdendritic region. Once the heat treatment temperature reached 1000 °C, the grain square was fully remodeled into the equiaxed grain, and an oversized quantity of solid solution precipitated at the interdendritic region. Because the heat treatment temperature rises, the coating grain square measure refined and the solid solution leaves the interdendritic region, leading to fine grain strengthening.

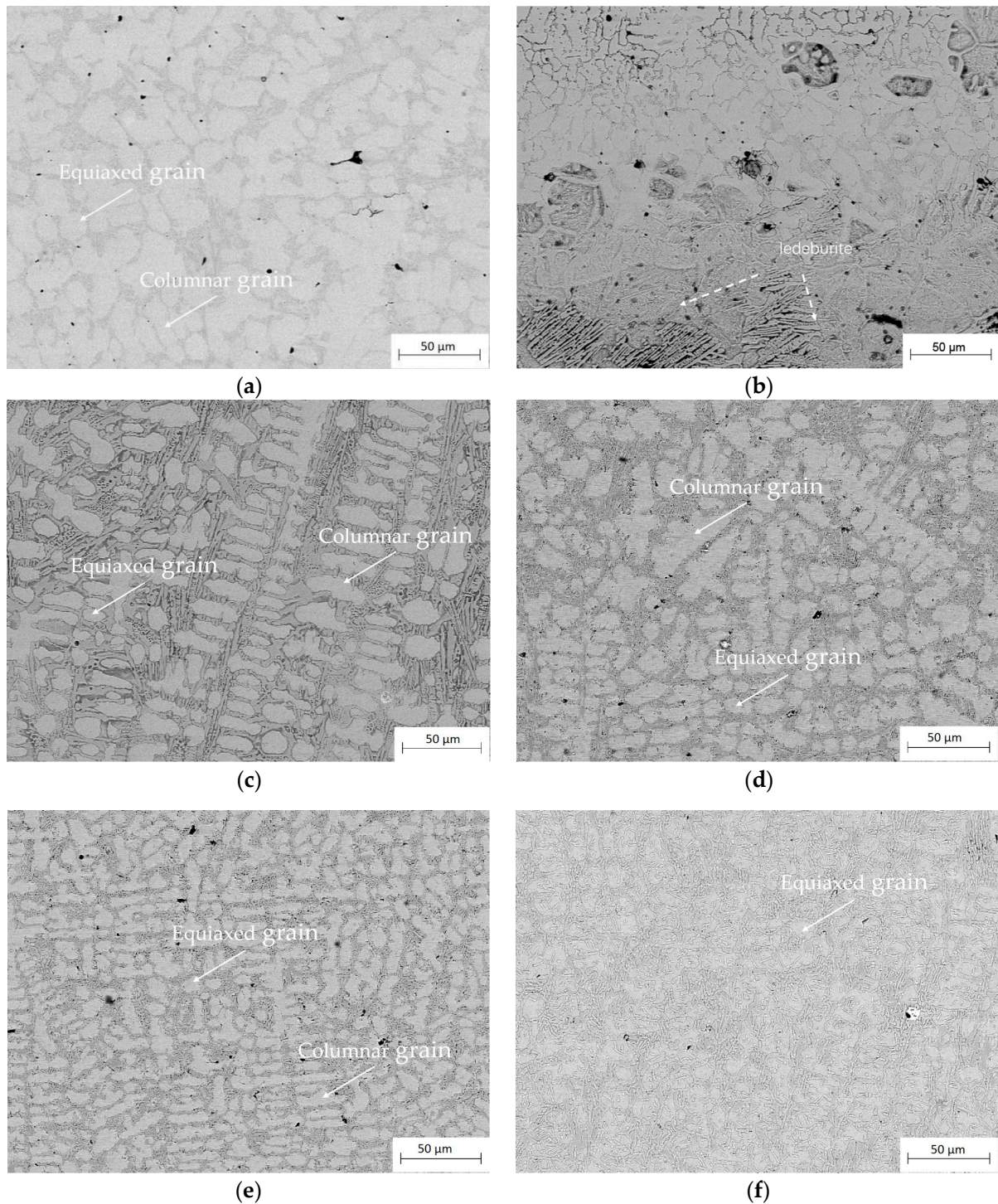


Figure 7. Cross-sectional microstructure of the as-cladded CoCrFeNiMn coating and the heat-treated ones in the middle part of the coating, (a) as-cladded; (b) transition zone; (c) 660 °C; (d) 780 °C; (e) 860 °C; (f) 1000 °C for 90 min.

Figure 8 shows the EDS mapping in the cross-section of the CoCrNiMn coatings after a 30-, 60-, and 90-min heat treatment at 780 °C and as-cladded coating. The results are summarized in Table 4. Table 4 shows the composition of the dendritic (DR) and interdendritic (ID) regions in the central part of the heat-treated and coated CoCrNiMn coatings. The interdendritic (ID) region was rich in Cr and Mn. Iron was evenly dispersed. The distribution and enrichment of Ni and Mn in the dendritic (DR) fraction was more homogeneous than in the ID region. Elemental point analysis shows that the content of nickel and manganese elements was much higher inside the grains than at the grain boundaries. Cobalt and nickel were more concentrated in the dendritic (DR) region, while the interdendritic (ID) region contained more chromium and manganese. The elemental distribution of the as-cladded and the heat-treated coatings was mostly consistent with a rise in Cr and Mn content at the interdendritic region of the coating. Even though there were variations within the selected areas between the as-cladded and heat-treated coatings, they were typically consistent in the elemental distributions. As seen in Table 4, the Cr and Mn content of the coating were enriched considerably at the interdendritic region once heat treated with a tiny low increase of Co and Ni elements at the dendritic region.

Table 4. Point analysis of elements in the middle part of the CoCrFeNiMn coating.

| Coatings | Weight Percent/wt.% | Region | Cr | Mn | Fe | Co | Ni |
|------------------------------|---------------------|------------------|--------|--------|--------|--------|-------|
| As-cladded | | 1-Dendritic | 3.230 | 5.255 | 77.150 | 6.675 | 7.690 |
| | | 2-Interdendritic | 12.031 | 9.123 | 72.913 | 3.413 | 2.520 |
| 30 min heat-treated coatings | | 3-Dendritic | 3.416 | 4.441 | 76.421 | 7.055 | 8.667 |
| | | 4-Interdendritic | 12.147 | 9.255 | 69.357 | 4.695 | 4.546 |
| 60 min heat-treated coatings | | 5-Dendritic | 3.731 | 5.687 | 73.883 | 7.211 | 9.488 |
| | | 6-Interdendritic | 11.992 | 10.308 | 68.424 | 4.523 | 4.753 |
| 90 min heat-treated coatings | | 7-Dendritic | 4.050 | 6.850 | 68.810 | 10.415 | 9.875 |
| | | 8-Interdendritic | 16.815 | 12.730 | 64.300 | 3.435 | 2.720 |

Figure 9 shows the microstructure of the coatings in high resolutions through TEM. There were large black square solid solutions formed within the coating. The grain size of the equiaxial crystals in the coating was refined, and the grain distribution was uniform, while the size of the square solid solution at the grain boundaries increased. Selected area diffraction patterns (SADPs) in the as-cladded CoCrFeNiMn coating confirmed that the as-cladded CoCrFeNiMn was composed of FCC solid-solution phase on the other hand. The electron diffraction patterns in the chosen area, as illustrated in Figure 9d, revealed that the diffraction spots in semicontinuous circles were composed of grain boundaries with high angles of misorientation. The detected spot indices were consistent with the FCC phase structure. The coating presented an oversized quantity of patterned black solid solution after heat treatment. The grain size of the coating was refined after heat treatment, mainly due to the solid solution of the microstructure after heat treatment, and the elements inside the grains were dispersed toward the interdendritic area. The SADPs, as shown in Figure 9, made sure that the heat-treated CoCrFeNiMn coatings were composed of the FCC phase once more. The coatings had a single FCC phase both in the as-cladded and heat-treated ones. The lattice parameters of (111) peak of the as-cladded coating and the heat-treated one at 780 °C for 90 min were 3.60061 Å and 3.59217 Å measured through a TEM diffraction pattern.

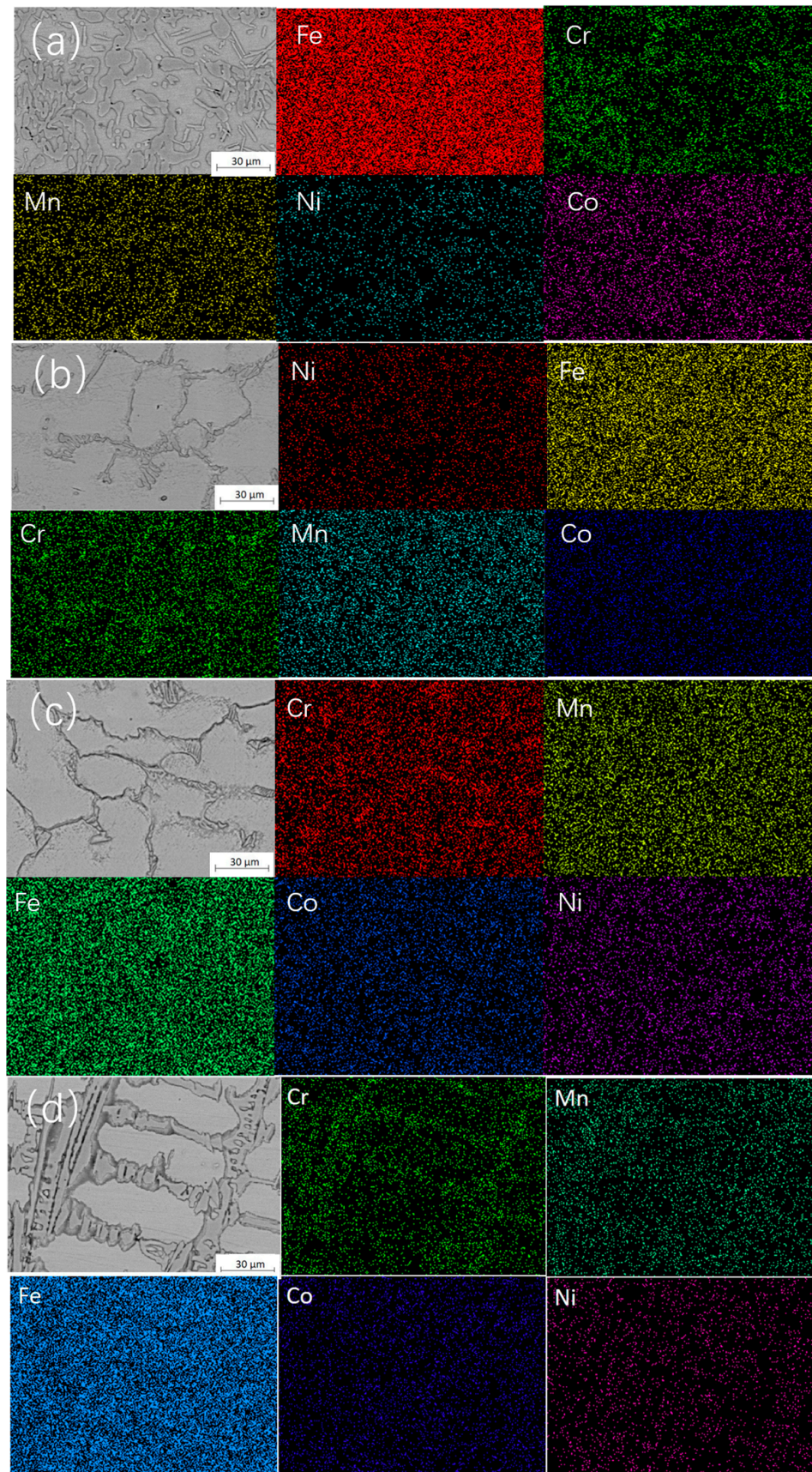


Figure 8. Cross-sectional distribution of elements in the CoCrFeNiMn coatings (a) as-cladded; (b) 780 °C for 30 min; (c) 780 °C for 60 min; (d) 780 °C for 90 min.

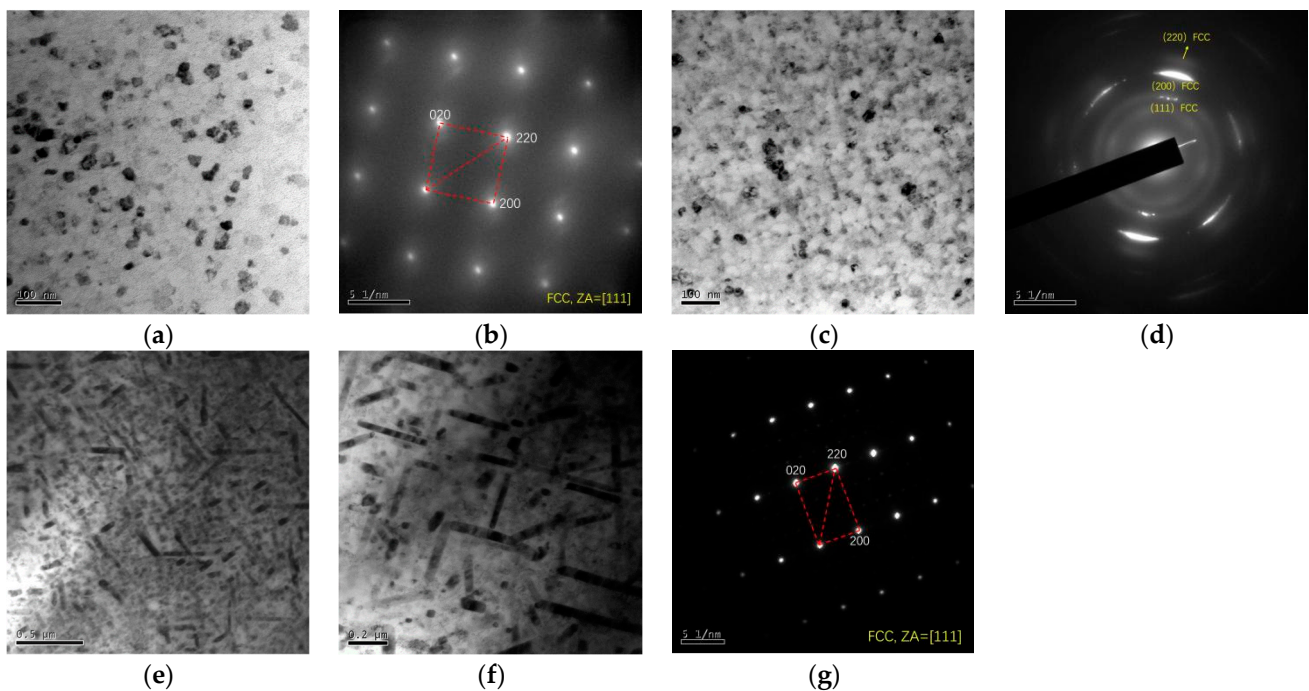


Figure 9. Microstructure analysis of the CoCrFeNiMn coating (a,c) bright-field TEM images of the as-cladded CoCrFeNiMn coating; (b,d) selected area electron diffraction patterns; (e,f) bright-field TEM images of the CoCrFeNiMn coatings after heat treatment at 780 °C for 90 min; (g) selected area electron diffraction patterns.

3.2. Phases

Figure 10 shows the XRD patterns of the CoCrFeNiMn coatings and the heat-treated ones with three major characteristic peaks at 2θ angles of 43.23° , 52.69° , and 73.60° . The characteristic peaks corresponded to the results of D.Y. Lin et al. [33] and (111), (200), and (220), showing lattice planes in a face-centered cuboidal (FCC) solution with PDF card no. 33-0397. The coating consisted of a stable single-solution phase both in the as-cladded and heat-treated ones. The formation of the single-FCC phase was attributed to the high structural entropy of the five elements in the alloy, which results in a high entropy alloy with a low Gibbs free energy, favoring the maintenance of a single-phase structure for the alloy system [34]. According to physical science relations, the Josiah Willard Gibbs free energy ($\Delta G_{\text{mix}} = \Delta H_{\text{mix}} - T \times \Delta S$) changed, and there was an outsized negative compound therapy among the elements of the system thanks to the quantitative isoatomic relation of the mixed system, wherever the H and entropy changed reciprocally [35]. The (111) peak exhibited the strongest diffraction intensity among all peaks, which meant a discriminatory growth of the crystal in this parallel direction. The intensity of the (111) and (200) peaks increased significantly with increasing heat treatment temperature, while the intensity of the (220) peak decreased. With magnified 2θ varied from 42° to 45° , as seen in Figure 10b, the (111) peak increased and became wide gradually with the increase of the temperature, which indicated that the increase of heat treatment temperature resulted in a slight decrease in grain spacing and a refinement of grain size [36]. Once heat treatment was performed between 660°C and 860°C , a tiny low peak appeared on the proper aspect of (111) and exaggerated gradually in intensity. However, the (111) peak disappeared once the temperature exceeded 1000°C , which was attributed to recrystallization that occurred at 1000°C . Since the manganese component has always had a low saturated vapor pressure and a high capacity for deoxygenation and slag removal, it has the highest rate of combustion loss and a large amount of volatiles in the same environment. Meanwhile, the experiments were conducted in a full argon environment throughout the heat treatment to prevent oxidation [37]. Therefore, no oxidization peaks existed in the XRD patterns.

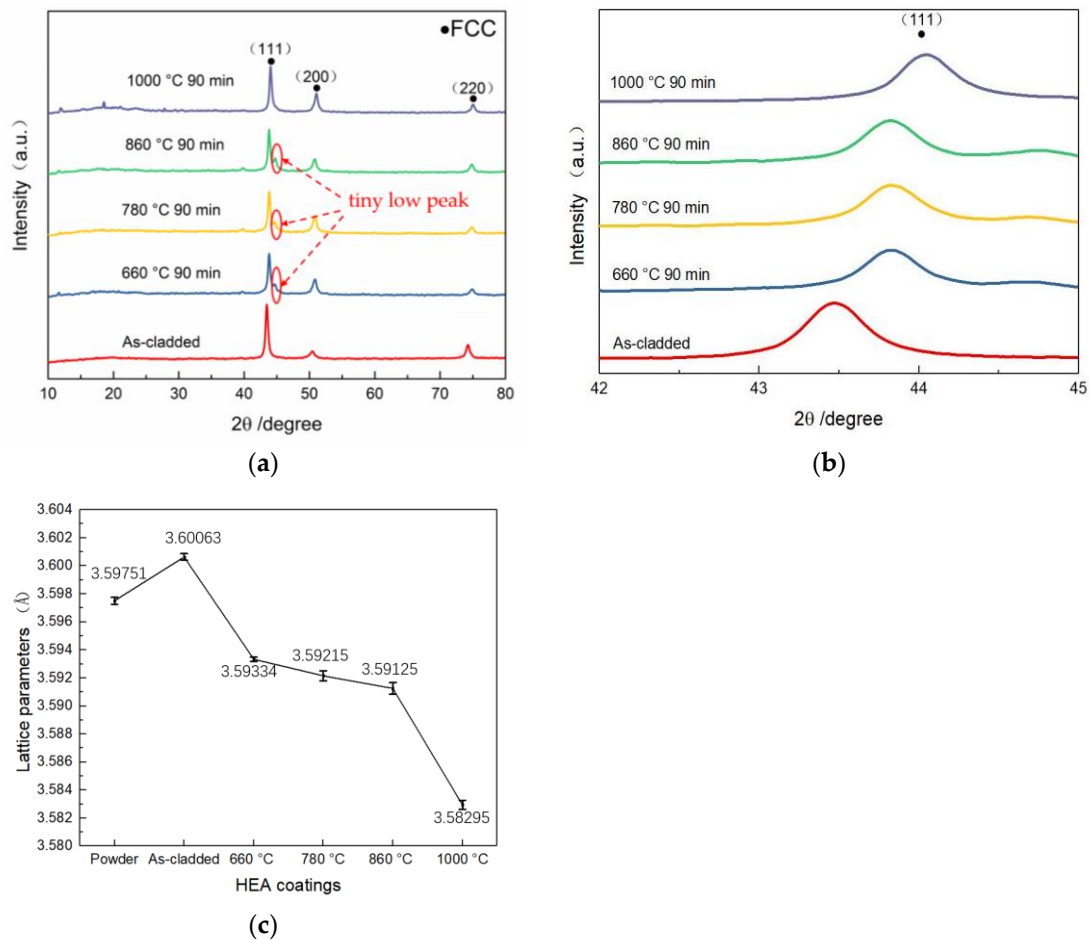


Figure 10. XRD analysis of the CoCrFeNiMn coating, (a) XRD patterns of the CoCrFeNiMn coatings and the heat-treated ones, (b) magnified view of the area with 2θ ranging from 40° to 48° , (c) lattice parameter of (111) peak of the CoCrFeNiMn powder and coatings.

The lattice parameter of the phases was calculated from the Scheler equation in the X-ray diffraction pattern, and the results are shown in Figure 10c. It was found that the lattice parameter decreased from 3.59334 \AA , 3.59215 \AA , 3.59125 \AA to 3.58295 \AA with the increase in heat treatment temperature. The powder's lattice parameter was 3.59751 \AA and the as-cladded coating's lattice parameter was 3.60063 \AA . The lattice parameter (111) peaks of the as-cladded coating and the heat-treated one at 780°C for 90 min were 3.60061 \AA and 3.59217 \AA , respectively, measured through TEM diffraction pattern, which basically corresponded to the results (3.60063 \AA for the as-cladded one and 3.59215 \AA for the heat-treated one at 780°C for 90 min) calculated from the Scheler equation in the X-ray diffraction pattern. When the plasma arc current was 65 A, the heat input of the plasma cladding was larger and the heating rate as well as cooling rate of the protective cladding method accelerated. The supercooling resulted in the CoCrFeNiMn HEA coating with more solid solutions, which eventually prompted a coating with a lattice parameter larger than that of the powder. During the heat treatment processing, the coating's desolvation rate increased and led to lower lattice parameters. Additionally, it has conjointly been reported that the decline of the lattice constant was attributed to the precipitation of excess substance atoms [38] and reduce of stress concentration [39].

3.3. Microhardness

As can be seen in Figure 11, the microhardness of the heat-treated coating was significantly higher than that of the as-cladded. In the original heating time of 30 min, the heated HEA coatings' microhardness increased with the rise in the heat treatment tempera-

ture. Meanwhile, with the prolongation of heat treatment time to 90 min, the heated HEA coatings' microhardness increased significantly. When the heat treatment temperature was increased to 660 °C, the microhardness of the coating showed a sharp increase, and when the temperature was increased from 660 °C to 860 °C, the microhardness of the coating decreased. When the temperature was increased to 1000 °C, the microhardness of the coating increased again. When the CoCrFeNiMn coating was heat treated at 660 °C for 90 min, it exhibited the highest microhardness of $563 \pm 6.9 \text{ HV}_{0.2}$. During heat treatment, some elements may separate and precipitate from the solid solution, which would partially weaken the solid solution strengthening effect. Meanwhile, with the rise of temperature, the coating grains were refined bit by bit accompanied by a fine grain reinforcement effect. Meanwhile, there were {Fe-Cr} precipitations along the coating's grain boundaries, similar to Ye's work [40] and Zhang's results [41], which contributed to the coating's high microhardness mainly. In Shim's work [42], the microhardness varied from 213 Hv (for Cu+Mn-rich FCC) to 325 Hv (Cr+Fe-rich BCC). As seen in Figure 11, the precipitation of solid solution at the grain boundaries of the coating would enhance the microhardness principally for the grain boundary precipitation strengthening.

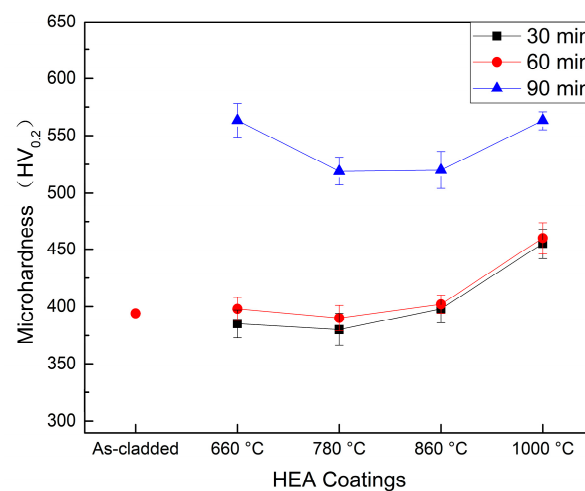


Figure 11. Cross-sectional distribution of microhardness in the as-cladded CoCrFeNiMn and the coatings after heat treatment.

Combined with the SEM image, the analysis of the precipitation of solid solution at the grain boundaries incorporated an improvement of the coating microhardness.

3.4. Wear Resistance

Figure 12 shows the frictional coefficient and the average frictional coefficient of the as-cladded CoCrFeNiMn coating and the heat-treated ones. The frictional coefficient increased sharply in the initial running-in stage and tended to be stable. At the start, the frictional coefficient was low because of the presence of associated oxide film on the surface of the coating. However, with the prolongation of the friction time, the oxide film was destroyed [42]. The initial low frictional coefficient was attributed to the reaction of the coating surface, wherever a skinny oxide film was present. Once the oxide film was destroyed by slippery resistance, there would be adhesive wear between the coating surface and friction components so that the friction became incredibly severe and the frictional coefficient increased sharply. At an equivalent time, the friction heat promoted the formation of associated oxide film on the surface of the coating, and these oxide films have a certain self-lubricating ability, which led to a slight decrease in the frictional coefficient. Oxide film in the wear process continues to experience formation and destruction. Once this dynamic cycle reaches equilibrium, the frictional resistance between the coating and the counterpart will be maintained at a constant value, and the coefficient of friction will also tend to stabilize [43]. The fluctuations that existed within the stable section of the

frictional coefficient were primarily associated with instrument vibration and measuring accuracy. The typical frictional coefficient of the as-cladded and heat-treated coatings at 660 °C, 780 °C, 860 °C, and 1000 °C were 0.7, 0.72, 0.75, 0.80, and 0.95, respectively. The heat-treated coatings at 1000 °C had the highest friction coefficient and the greatest fluctuations. The coatings heat-treated at 780 °C and 860 °C had slightly lower frictional coefficients; however, they were considerably higher than those of the as-cladded and heat-treated one at 660 °C. The as-cladded coating had the lowest frictional coefficient. Meanwhile, the heat-treated coating at 660 °C had the best lubricity.

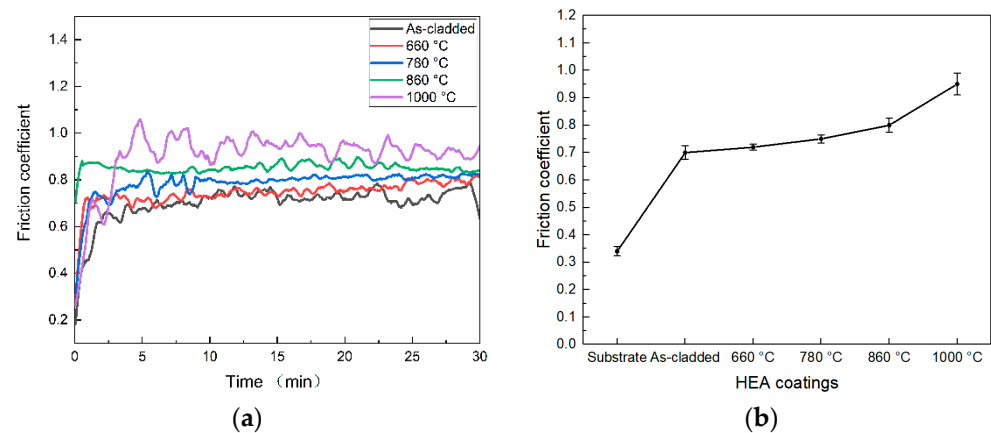


Figure 12. (a) Friction coefficient of the as-cladded coating and the coatings after heat treatment, (b) The average friction coefficient of the as-cladded coating and the coatings after heat treatment.

Figure 13 shows the wear mass loss of the as-cladded CoCrFeNiMn coatings, heat-treated ones, and N80 counterparts after wear tests. As the width of the coating's wear scar was not uniform, the wear mass loss was converted into a comparative analysis of the quality loss for the same width of the wear scars. At heat treatment temperatures of 660 °C, 780 °C, and 860 °C, the wear resistance of the coating was superior to that of the as-cladded coatings. The wear resistance of the heat-treated coatings was optimized at a heat treatment temperature of 660 °C. The lower the wear mass of the coating, the higher its wear resistance under the same wear conditions. There was a linear relationship between microhardness and the wear resistance of the material. The microhardnesses of the heat-treated coatings were all higher than that of the cladding. It is noteworthy that the microhardness of the coatings was highest at the heat treatment temperature of 1000 °C, but the wear mass loss of the coatings increased sharply to 15.52 mg, and their friction coefficients were also the highest, with the largest fluctuation of the friction coefficients. The solid solution of the 1000 °C heat-treated coating was the thickest and most varied. These strips and irregular {Fe-Cr} solid solutions varied in microhardness from the substrate and underneath the action of the resistance load, which led to an asynchronous degree of wear and tear, successively developed into an outsized number of uneven microsurfaces, resulting in a rise within the wear quantity of the coating. The degree of wear and tear was coupled with the resistance of the contact space. With the increase of the frictional resistance, the shear stress on the coating surface particles would increase, leading to the coating surface particles being vulnerable to wear out. The frictional coefficient of the coating was additionally related to phase changes and microhardness variations.

Macroscopic track morphologies of the CoCrFeNiMn coatings after heat treatment are shown in Figure 14. The overall comparison shows that the width of the coating wear track was relatively uniform, about 3 mm. However, when the heat treatment temperature was 660 °C, 780 °C, and 860 °C, the morphology of the coating wear track was relatively uniform, and the heat treatment temperature increased to 1000 °C. The furrow distribution and width of the coating wear features were uneven, which was combined with the analysis of the coating structure above. It was mainly caused by high-temperature heat treatment that changes the microstructure of the coating.

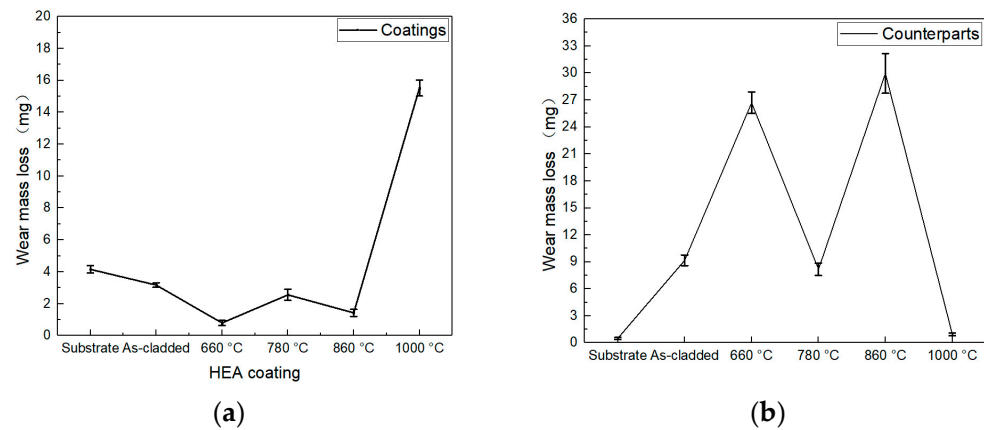


Figure 13. Wear mass loss of the CoCrFeNiMn coatings and N80 counterparts. (a) wear mass loss of the CoCrFeNiMn coatings; (b) wear mass loss of the N80 counterparts.

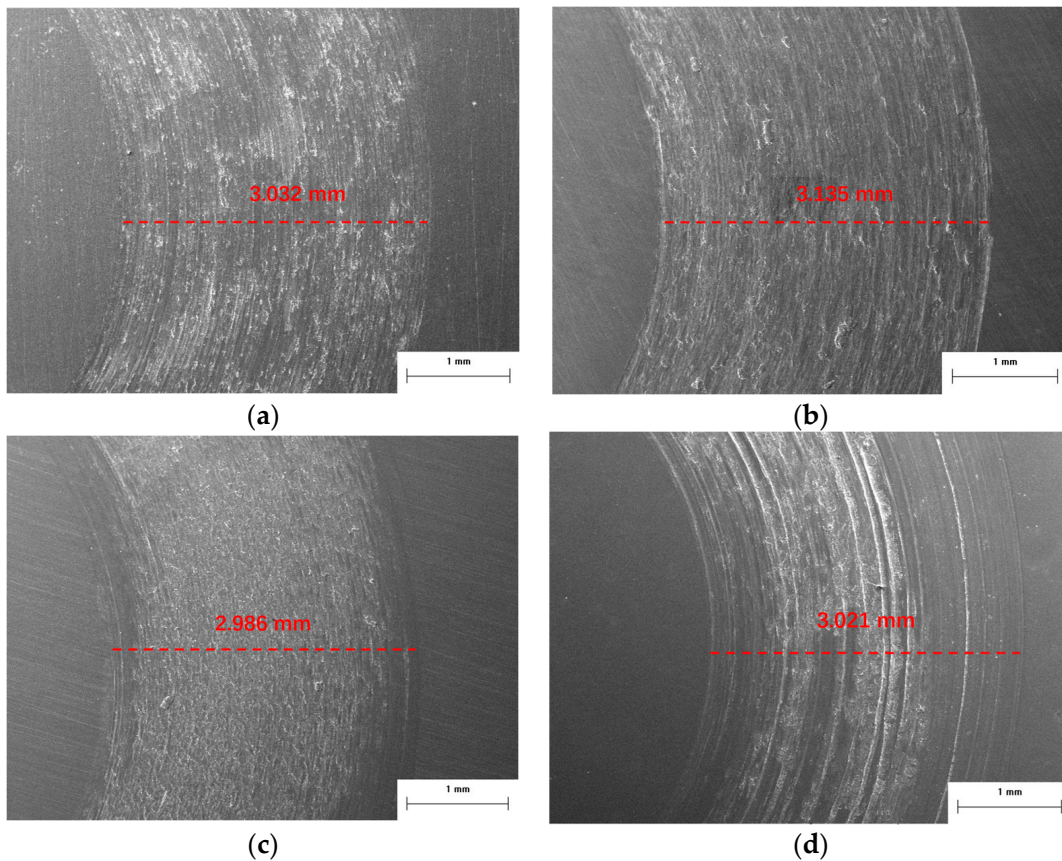
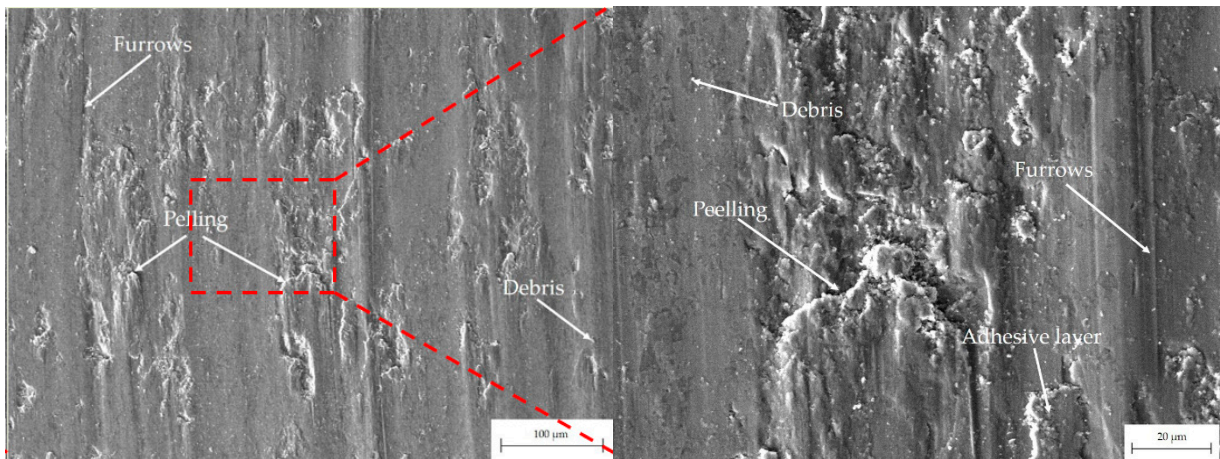
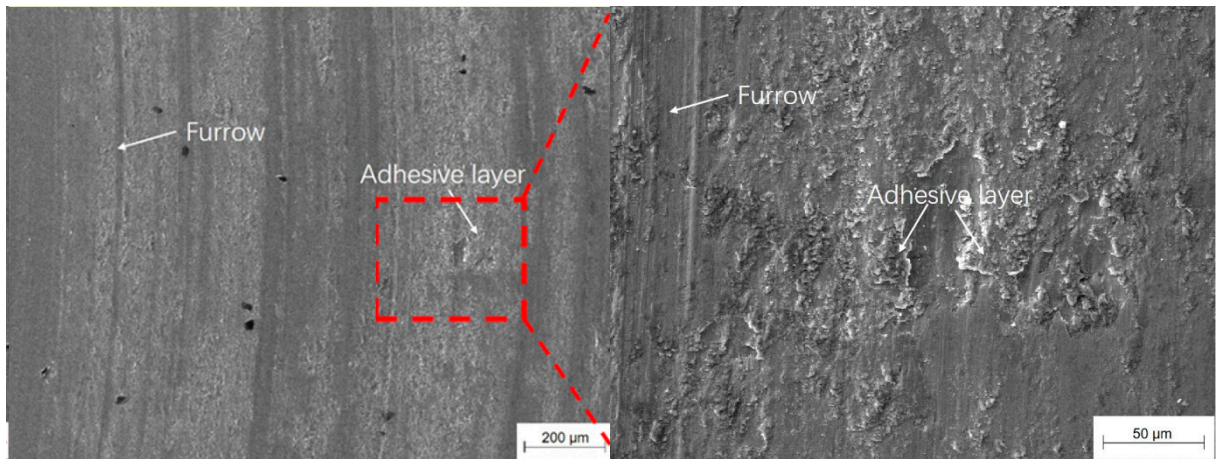


Figure 14. Macroscopic track morphologies of the CoCrFeNiMn coatings after heat treatment: (a) 660 °C, (b) 780 °C, (c) 860 °C, (d) 1000 °C.

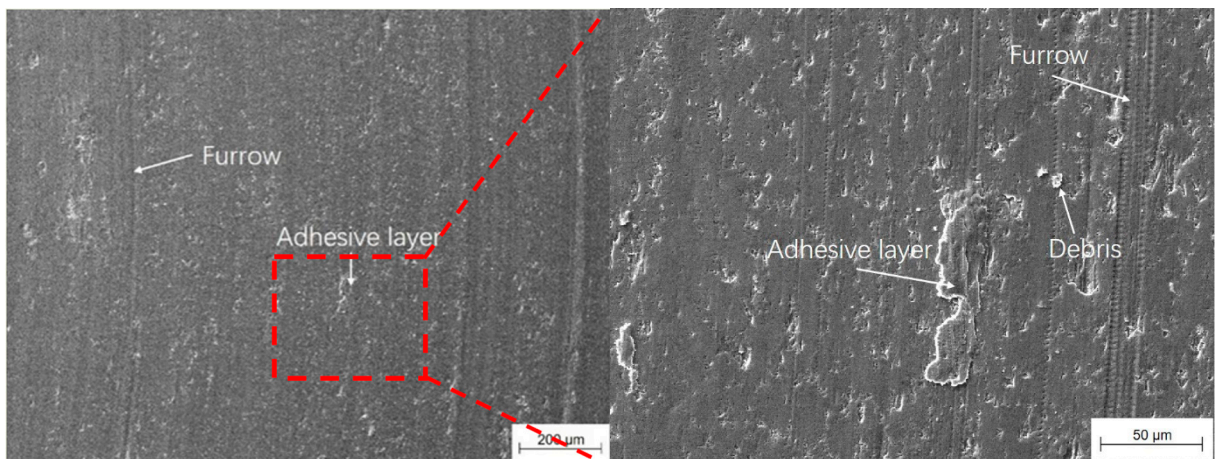
The worn surface of the as-cladded coating consists mainly of furrows, spalling, wear particles, and adhesive layers as shown in Figure 15. As the heat treatment temperature increased, the depth of the furrows on the worn surface increased, the degree of flaking increased, and the wear resistance of the coating decreased. When the temperature was 660 °C, the worn surface of the coating became relatively flat. After heat treatment at 780 °C, the wear scars of the coating show shallow furrows and a small amount of adhesion, as shown in Figure 15c. The wear scars of the heat-treated coating at 800 °C were uneven furrows with a lot of flaking and adhesion.



(a)

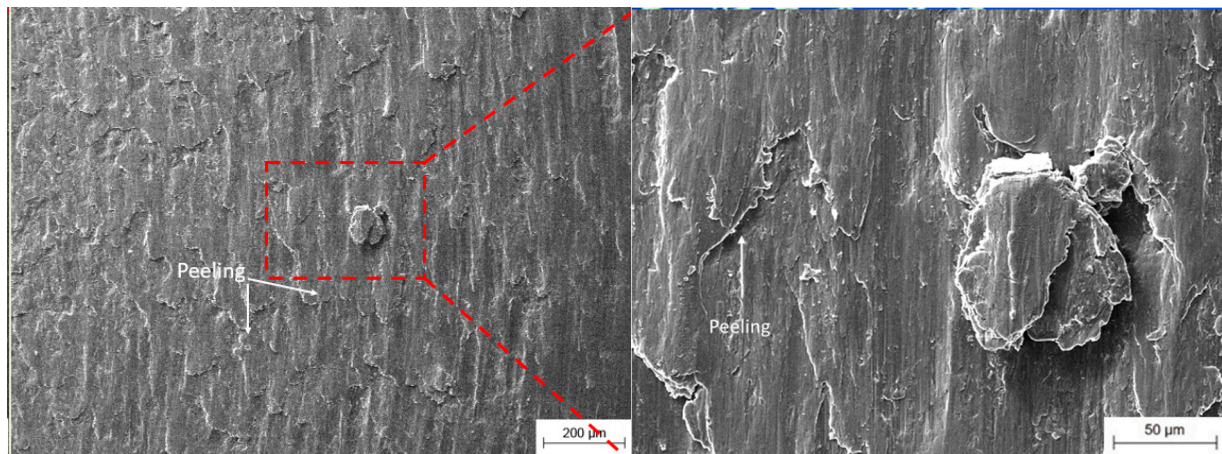


(b)

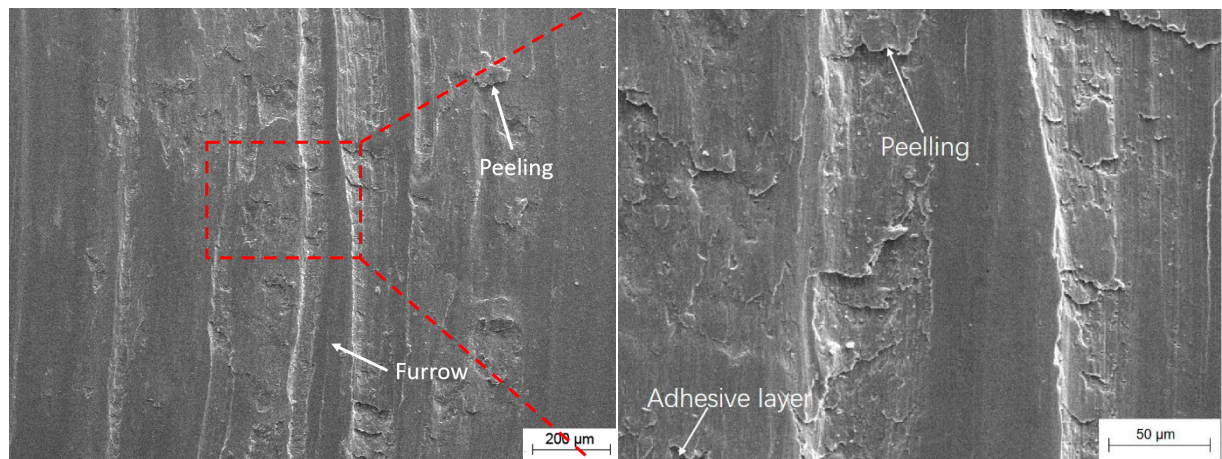


(c)

Figure 15. Cont.



(d)



(e)

Figure 15. Wear morphologies of the as-cladded CoCrFeNiMn coating (a) the heat-treated ones at (b) 660 °C, (c) 780 °C, (d) 860 °C, (e) 1000 °C for 90 min.

The surface ESD map of the coating wear surface is shown in Figure 16. By EDS surface scanning analysis on the micro area of the wear surface, it is found that there are a large number of iron-containing oxides on the surface of the wear fold layer. The oxygen atom is distributed in the main surface of the fold, and the oxygen atom content in the furrow is low, which proves that the oxide layer formed during the wear process has oxidative wear.

After heat treatment at 1000 °C, the roughness of the wear surface was the greatest, and the furrows were deep and wide, but the flaking and adhesion were weakened, as shown in Figure 17. The coating was subjected to axial and tangential forces exerted by the N80 counterpart, resulting in the formation of grooves on its surface due to microcutting. As a result of the inertial and tangential forces, the broken metal parts were distributed on both sides of the grooves, forming wear debris. Typical localized high temperatures lasted only some milliseconds. At this moment, the coating's surface chemical compound was broken and adhered to at the contacting zone. Meanwhile, the metal on the surface would be torn apart, forming abrasive particles, which would conjointly flake during the contacting and wearing between the wear surface of the coating and the counterpart. Some metal particles adhered to the surface of another metal, forming adhesive wear. The mechanism of adhesive wear could be cycles of adherence, destruction, and re-adhesion. All varieties of wear included plastic deformation, adhesive wear, abrasive wear, and spalling. Since the cladding layer had a single FCC phase with relatively low microhardness, it had plastic

deformation adhesive wear, groove wear, and spalling throughout the wear. Oxidization particles formed on the worn surface under high temperatures. Consequently, adhesive, abrasive, and mild oxidative wear were the main wear mechanisms of the coating.

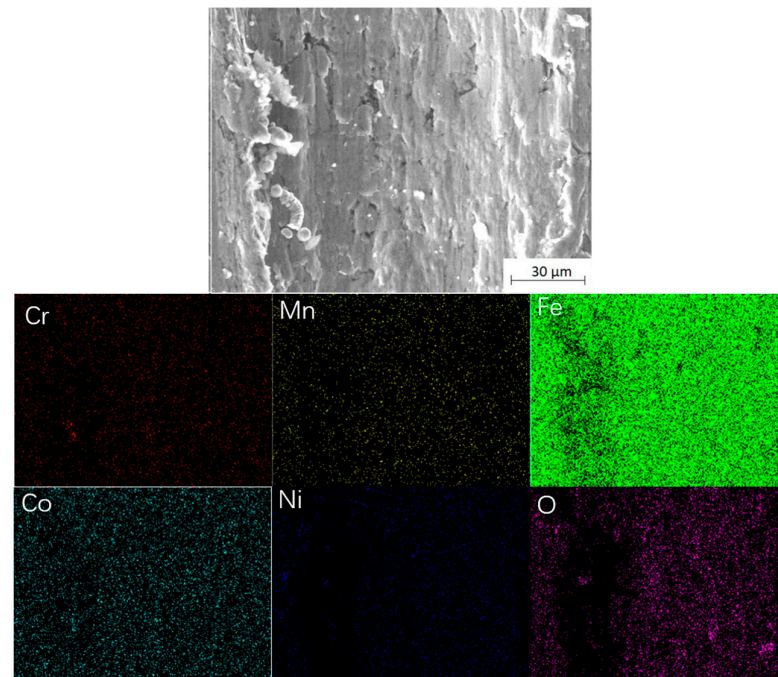


Figure 16. EDS map of the CoCrFeNiMn as-cladded coating wear surface.

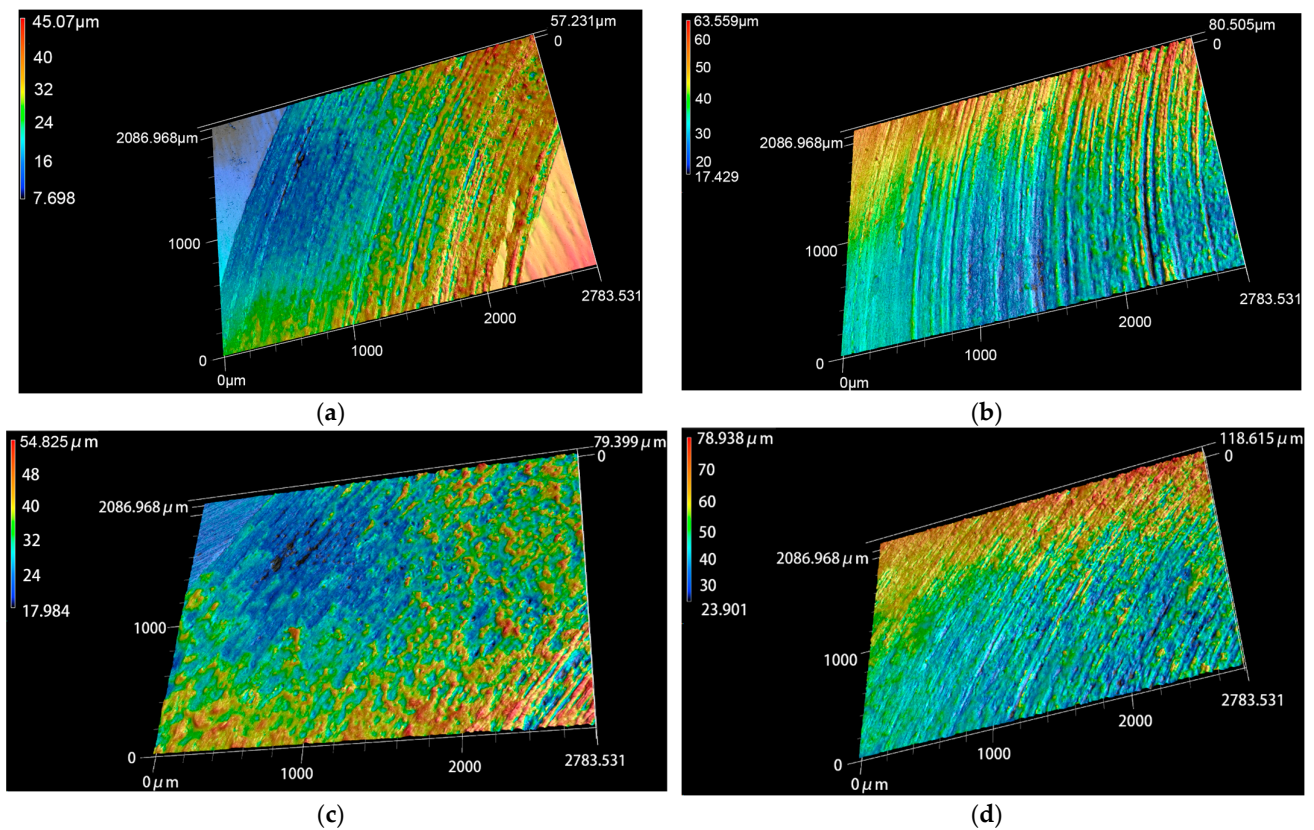


Figure 17. 3D morphologies of the CoCrFeNiMn coatings after heat treatment: (a) 660 °C, (b) 780 °C, (c) 860 °C, (d) 1000 °C.

Figure 18 displays the wear schematic diagram of the CoCrFeNiMn coatings. During the initial stages of the friction and wear test, the oxide film on the alloy surface was disrupted, and abrasive chips were introduced by the microcutting force of the pin. As the friction test progressed, the abrasive chips migrated across the friction surface and accumulated towards the cratered area, forming an adhesive under the pressure of the pin. The pin's microcutting power subjected the raised areas of the coating surface to transverse shear forces, resulting in crack formation and extension. As the friction time increased, the pin covered more distance on the coating surface, and abrasive chips gradually covered the friction surface of the coating. During partially oxidative wear, the migration of abrasive chips occurs continuously as the pin slides, resulting in a gradual decrease in wear loss. The pins cause microcutting, generating chips and abrasives on the coating's surface, which leads to a small amount of flaking of the coating. The pin's constant movement generated low amplitude vibrations in the cracks, cratered areas, spalling, and raised areas of the coating surface, causing damage to the coating. The cracks on the coating surface expanded under continuous cyclic stress until spalling occurred, resulting in the formation of spalling craters. Cracks continued to appear on the coating surface during the pin's movement. As cracks develop and close, they can cause spalling pits when peeled off. The counterpart pin's continuous movement causes abrasive chips to move across the coating's surface, adhering to the cratered area and creating an adhesive.

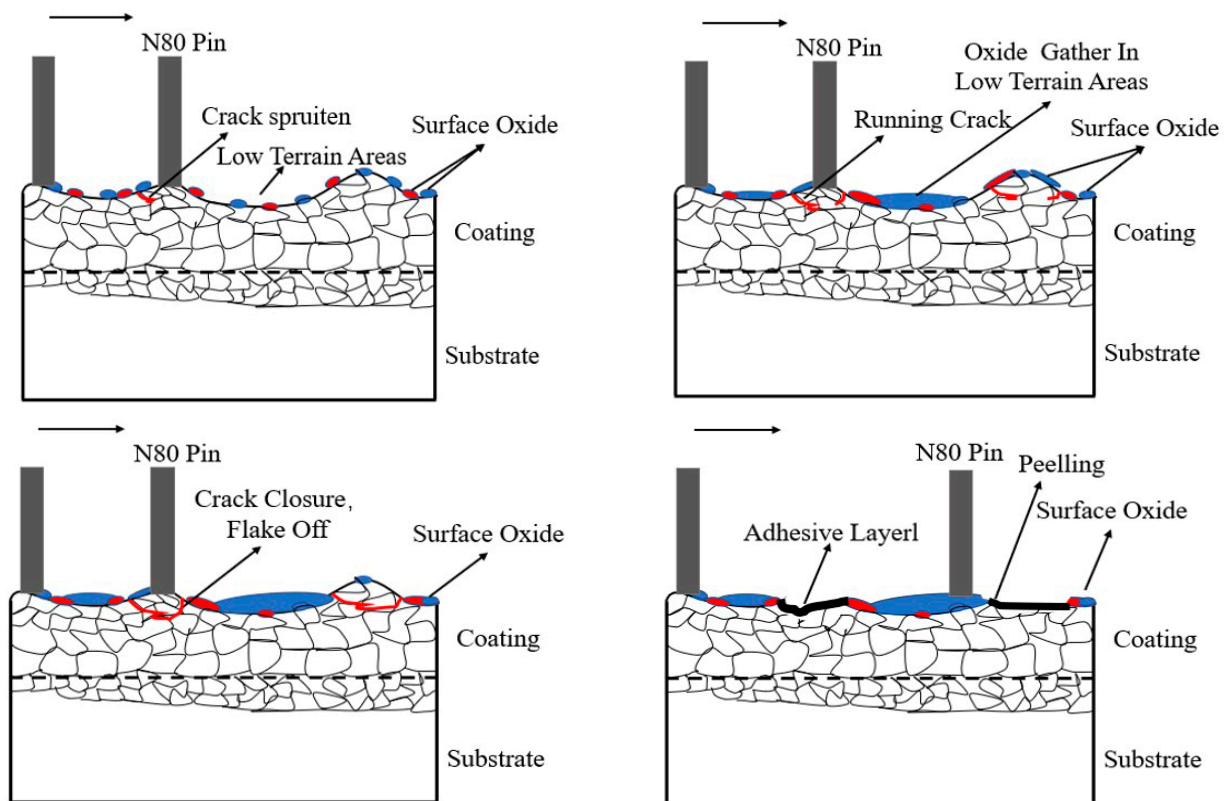


Figure 18. Wear schematic diagram of the CoCrFeNiMn coatings.

4. Conclusions

This work investigated the effects of the heat treatment process on the phase composition, microstructure, and properties of CoCrFeNiMn coatings through plasma transfer arc cladding on compacted graphite iron. Several conclusions were drawn as follows:

1. After heat treatment with argon as a protection gas, the CoCrFeNiMn coatings were kept with a single FCC phase structure. The grain size of the coating became refined with smaller dendrites, larger dendritic spacing, and more Cr-rich compounds precipitated between dendrites than the as-cladded one.

2. The CoCrFeNiMn coating's microhardness improved significantly through heat treatment. Following a 30-min heat treatment at 660 °C for the coating, it had a maximum microhardness of 563 ± 6.9 HV_{0.2}, 1.46 times the as-cladded one.

3. When the coating was heat treated at 660 °C for 30 min, it had the lowest frictional coefficient, the smallest wear mass loss, and the greatest wear resistance. It greatly strengthened and increased wear protection on compacted graphite iron.

4. The CoCrFeNiMn coating exhibited adhesive wear, abrasive wear, and oxidative wear. The CoCrFeNiMn coating exhibited less friction and wear damage as well as better durability than compacted graphite iron.

Author Contributions: Conceptualization, B.Z., R.F., P.G., B.C. and J.L. (Jianping Li); methodology, B.Z., R.F., P.G., B.C., F.L., D.Z. and A.N.; software, P.G., R.F., B.C. and Y.G.; validation, P.G., B.C., and B.Z.; formal analysis, B.Z., P.G., R.F., B.C. and Z.Y.; investigation B.Z., R.F., P.G., B.C., F.L., D.Z., J.G., L.C., J.L. (Jiawei Liu) and Y.L.; data curation, Z.Y.; writing—original draft preparation, R.F.; writing—review and editing, P.G.; project administration, J.L. (Jianping Li); funding acquisition, P.G. and J.L. (Jianping Li). All authors have read and agreed to the published version of the manuscript.

Funding: This work was funded by the National Natural Science Foundation of China (51771140), Foreign Experts Program of the Ministry of Science and Technology (G2022040016L), The Youth Innovation Team of Shaanxi Universities: Metal Corrosion Protection and Surface Engineering Technology, Research and application of key component materials for engines, Shaanxi Provincial Natural Science Foundation (2023-JC-YB-380), Shaanxi Provincial Key Research and Development Project (2019ZDLGY05-09, 2022GY-404), and Xi'an Science and Technology Plan Project (23LLRHZDZX0019, 23GXFW0036).

Institutional Review Board Statement: Not applicable.

Informed Consent Statement: Not applicable.

Data Availability Statement: Data are contained within the article.

Acknowledgments: We thank Hongbo Duan for the characterization of wear scars.

Conflicts of Interest: Authors Lei Cheng, Jinyuan Gong, Jiawei Liu and Yu Li were employed by the company Shaanxi North Dynamic Co., Ltd. The remaining authors declare that the research was conducted in the absence of any commercial or financial relationships that could be construed as a potential conflict of interest.

References

1. Yeh, J.W.; Chen, S.K.; Lin, S.J.; Gan, J.Y.; Chin, T.S.; Shun, T.T.; Tsau, C.H.; Chang, S.Y. Nanostructured High-Entropy Alloys with Multiple Principal Elements: Novel Alloy Design Concepts and Outcomes. *Adv. Eng. Mater.* **2004**, *6*, 299–303. [[CrossRef](#)]
2. Yeh, J.W. Physical metallurgy of high-entropy alloys. *J. Miner. Met. Mater. Soc.* **2015**, *67*, 2254–2261. [[CrossRef](#)]
3. Ma, Y.; Wang, Q.; Jiang, B.B.; Li, C.L.; Hao, J.M.; Li, X.N.; Dong, C.; Nieh, T.G. Controlled formation of coherent cuboidal nanoprecipitates in body-centered cubic high-entropy alloys based on Al₂(Ni, Co, Fe, Cr)₁₄ compositions. *Acta Mater.* **2018**, *147*, 213–225. [[CrossRef](#)]
4. Zhang, Y.; Gao, M.C.; Dahmen, K.A.; Liaw, P.K.; Lu, Z.P. Microstructures and properties of high-entropy alloys. *Prog. Mater. Sci.* **2014**, *61*, 1–93. [[CrossRef](#)]
5. Tong, Z.P.; Liu, H.L.; Jiao, J.F.; Zhou, W.F.; Yang, Y.; Ren, X.D. Improving the strength and ductility of laser directed energy deposited CrMnFeCoNi high-entropy alloy by laser shock peening. *Addit. Manuf.* **2020**, *35*, 101417. [[CrossRef](#)]
6. Fu, Z.; Jiang, L.; Wardini, J.L.; MacDonald, B.E.; Xiong, H.W.; Zhang, D.; Zhou, Y.; Rupert, T.J.; Chen, W.; Lavernia, E.J. A high-entropy alloy with hierarchical nano-precipitates and ultrahigh strength. *Sci. Adv.* **2018**, *4*, 8712. [[CrossRef](#)]
7. Zou, Y.; Ma, H.; Spolenak, R. Ultrastrong ductile and stable high-entropy alloys at small scales. *Nat. Commun.* **2015**, *6*, 7748. [[CrossRef](#)]
8. Yao, Y.; Huang, Z.; Xie, P.; Lacey, S.D.; Jacob, R.J.; Xie, H.; Chen, F.; Nie, A.; Pu, T.; Rehwoldt, M.; et al. Carbothermal shock synthesis of high-entropy-alloy nanoparticles. *Science* **2018**, *359*, 1489–1494. [[CrossRef](#)]
9. El-Atwani, O.; Li, N.; Li, M.; Devaraj, A.; Baldwin, J.K.S.; Schneider, M.M.; Sobieraj, D.; Wróbel, J.S.; Nguyen-Manh, D.; Maloy, S.A.; et al. Outstanding radiation resistance of tungsten-based high-entropy alloys. *Sci. Adv.* **2019**, *5*, 2002. [[CrossRef](#)]
10. Qiu, Y.; Thomas, S.; Gibson, M.A.; Fraser, H.L.; Birbilis, N. Corrosion of high entropy alloys. *Npj Mater. Degrad.* **2017**, *1*, 15. [[CrossRef](#)]
11. Chuang, M.; Tsai, M.; Wang, W.; Lin, S.; Yeh, J. Microstructure and wear behavior of Al_xCo_{1.5}CrFeNi_{1.5}Ti_y high-entropy alloys. *Acta Mater.* **2011**, *59*, 6308–6317. [[CrossRef](#)]

12. Kumar, S. Comprehensive review on high entropy alloy-based coating. *Surf. Coat. Technol.* **2024**, *477*, 130327. [[CrossRef](#)]
13. Arif, Z.U.; Khalid, M.Y.; ur Rehman, E.; Ullah, S.; Atif, M.; Tariq, A. A review on laser cladding of high-entropy alloys, their recent trends and potential applications. *J. Manuf. Process.* **2021**, *68*, 225–273. [[CrossRef](#)]
14. Cui, Y.; Shen, J.Q.; Geng, K.P.; Hu, S.S. Fabrication of FeCoCrNiMnAl_{0.5}-FeCoCrNiMnAl gradient HEA coating by laser cladding technique. *Surf. Coat. Technol.* **2021**, *412*, 127077. [[CrossRef](#)]
15. Chen, B.Y.; Gao, P.H.; Zhang, B.; Zhao, D.M.; Wang, W.; Jin, C.; Yang, Z.; Guo, Y.C.; Liang, M.X.; Li, J.P.; et al. Wear properties of iron-based alloy coatings prepared by plasma transfer arc cladding. *Coatings* **2022**, *12*, 243. [[CrossRef](#)]
16. Gao, P.H.; Fu, R.T.; Chen, B.Y.; Zeng, S.C.; Zhang, B.; Yang, Z.; Guo, Y.C.; Liang, M.X.; Li, J.P.; Lu, Y.Q.; et al. Corrosion Resistance of CoCrFeNiMn High Entropy Alloy Coating Prepared through Plasma Transfer Arc Claddings. *Metals* **2021**, *11*, 1876. [[CrossRef](#)]
17. Cheng, J.B.; Murakami, H.; Yeh, J.W.; Yeh, A.C. Kazuya Shimoda, On the study of thermal-sprayed Ni_{0.2}Co_{0.6}Fe_{0.2}CrSi_{0.2}AlTi_{0.2} HEA overlay coating. *Surf. Coat. Technol.* **2017**, *316*, 71–74.
18. Nikbakht, R.; Saadati, M.; Kim, T.S.; Jahazi, M.; Kim, H.S.; Jodoin, B. Cold spray deposition characteristic and bonding of CrMnCoFeNi high entropy alloy. *Surf. Coat. Technol.* **2021**, *425*, 127748. [[CrossRef](#)]
19. Zhao, Y.M.; Zhang, X.M.; Quan, H.; Chena, Y.J.; Wang, S.; Zhang, S. Effect of Mo addition on structures and properties of FeCoNiCrMn high entropy alloy film by direct current magnetron sputtering. *J. Alloys Compd.* **2022**, *895*, 162790. [[CrossRef](#)]
20. Zhao, Z.Z.; Meng, H.M.; Ren, P.W. CoNiWReP high entropy alloy coatings prepared by pulse current electrodeposition from aqueous solution. *Colloid Surf. A* **2022**, *648*, 129404. [[CrossRef](#)]
21. Zhao, L.; Zhang, F.; Wang, L.; Yan, S.; Yin, F. Effects of Post-Annealing on Microstructure and Mechanical Properties of Plasma Sprayed Ti-Si-C Com-posite Coatings with Al Addition. *Surf. Coat. Technol.* **2021**, *416*, 127164. [[CrossRef](#)]
22. Hong, D.; Huang, L.; Yuan, J.; Li, C. Influence of Annealing Temperature on Microstructure Evolution of TiAlSiN Coating and Its Tribological Behavior Against Ti₆Al₄V Alloys. *Ceram. Int.* **2021**, *47*, 3789–3796. [[CrossRef](#)]
23. Sha, M.; Li, F.; Zhang, J.; Na, L.; Ning, W. Effects of Annealing on the Microstructure and Wear Resistance of AlCoCrFeNiTi_{0.5} High-Entropy Alloy Coating Prepared by Laser Cladding. *Rare Met. Mater. Eng.* **2017**, *46*, 1237–1240.
24. Hao, E.; An, Y.; Liu, X.; Wang, Y.; Zhou, H.; Yan, F. Effect of Annealing Treatment on Microstructures, Mechanical Properties and Cavitation Erosion Performance of High Velocity Oxy-Fuel Sprayed NiCoCrAlYTa Coating. *J. Mater. Sci. Technol.* **2020**, *53*, 19–31. [[CrossRef](#)]
25. Lin, D.Y.; Zhang, N.N.; He, B.; Jin, B.Q.; Zhang, Y.; Li, D.Y.; Dong, F.Y. Influence of laser remelting and vacuum heat treatment on plasma-sprayed FeCoCrNiAl alloycoatings. *J. Iron Steel Res. Int.* **2017**, *24*, 1199–1205. [[CrossRef](#)]
26. Munitz, A.; Salhov, S.; Hayun, S.; Frage, N. Heat treatment impacts the micro-structure and mechanical properties of AlCoCrFeNi hightentropy alloy. *J. Alloys Compd.* **2016**, *683*, 221–230. [[CrossRef](#)]
27. Li, J.; Hui, J.; Lu, Y.P.; Wang, T.; Cao, Z.; Li, T. Mechanical properties improvement of AlCrFeNi₂Ti_{0.5} high entropy alloy through annealing design and its relationship with its particle-reinforced microstructures. *J. Mater. Sci. Technol.* **2015**, *31*, 397–402.
28. He, F.; Wang, Z.J.; Niu, S.Z.; Wu, Q.F.; Li, J.J.; Wang, J.C.; Liu, C.T.; Dang, Y.Y. Strengthening the CoCrFeNiNb_{0.25} high entropy alloy by FCC precipitate. *J. Alloys Compd.* **2016**, *667*, 53–57. [[CrossRef](#)]
29. Zhang, M.N.; Zhou, X.L.; Zhu, W.Z.; Li, J.H. Influence of annealing on microstructure and mechanical properties of refractory CoCrMoNbTi_{0.4} high-entropy alloy. *Metall. Mater. Trans. A* **2018**, *49*, 1313–1327. [[CrossRef](#)]
30. Zhang, C.; Wu, G.F.; Dai, P.Q. Phase transformation and aging behavior of Al_{0.5}CoCrFeNiSi_{0.2} high-entropy alloy. *J. Mater. Eng. Perform.* **2015**, *24*, 1918–1925. [[CrossRef](#)]
31. Niu, S.; Kou, H.; Tong, G.; Yu, Z.; Wang, J.; Li, J. Strengthening of nanoprecipitations in an annealed Al_{0.5}CoCrFeNi high entropy alloy. *Mater. Sci. Eng. A* **2016**, *671*, 82–86. [[CrossRef](#)]
32. Gao, P.H.; Fu, R.T.; Liu, J.L.; Chen, B.Y.; Zhang, B.; Zhao, D.M.; Yang, Z.; Guo, Y.C.; Liang, M.X.; Li, J.P.; et al. Influence of Plasma Arc Current on the Friction and Wear Properties of CoCrFeNiMn High Entropy Alloy Coatings Prepared on CGI through Plasma Transfer Arc Cladding. *Coatings* **2022**, *12*, 633. [[CrossRef](#)]
33. Lin, D.Y.; Zhang, N.; He, B.; Gong, X.; Zhang, Y.; Li, D.; Dong, F. Structural Evolution and Performance Changes in FeCoCr-NiAlNbx High-Entropy Alloy Coatings Cladded by Laser. *J. Therm. Spray Technol.* **2017**, *26*, 2005–2012. [[CrossRef](#)]
34. Wang, C.; Gao, Y.; Wang, R.; Wei, D.; Fu, Y. Microstructure of laser-clad Ni60 cladding layers added with different amounts of rare-earth oxides on 6063 Al alloys. *J. Alloys Compd.* **2018**, *740*, 1099–1107. [[CrossRef](#)]
35. Laplanche, G.; Berglund, S.; Reinhart, C.; Kostka, A.; Fox, F.; George, E. Phase stability and kinetics of sigma-phase precipitation in CrMnFeCoNi high-entropy alloys. *Acta Mater.* **2018**, *161*, 338–351. [[CrossRef](#)]
36. Li, H.G.; Huang, Y.J.; Zhao, W.J.; Chen, T.; Sun, J.F.; Wei, D.Q.; Du, Q.; Zou, Y.C.; Lu, Y.Z.; Zhu, P.; et al. Overcoming the strength-ductility trade-off in an additively manufactured CoCrFeMnNi high entropy alloy via deep cryogenic treatment. *Addit. Manuf.* **2022**, *50*, 102546. [[CrossRef](#)]
37. Wu, W.; Jiang, L.; Jiang, H.; Pan, X.; Cao, Z.; Deng, D.; Wang, T.; Li, T. Phase Evolution and Properties of Al₂CrFeNiMo_x High-Entropy Alloys Coatings by Laser Cladding. *J. Therm. Spray Technol.* **2015**, *24*, 1333–1340. [[CrossRef](#)]
38. Jiang, L.; Lu, Y.P.; Dong, Y.; Wang, T.M.; Cao, Z.Q.; Li, T.J. Annealing effects on the microstructure and properties of bulk high-entropy CoCrFeNiTi_{0.5} alloy casting ingot. *Intermetallics* **2014**, *44*, 37–43. [[CrossRef](#)]
39. Sathiyamoorthi, P.; Basu, J.; Kashyap, S.; Pradeep, K.G.; Kottada, R.S. Thermal stability and grain boundary strengthening in ultrafine-grained CoCrFeNi high entropy alloy composite. *Mater. Des.* **2017**, *134*, 426–433. [[CrossRef](#)]

40. Ye, F.; Jiao, Z.; Zhao, L. Effect of Y_2O_3 addition on the microstructure and properties of Ni60 additives by micro-plasma cladding. *Mater. Res. Express* **2019**, *6*, 026562. [[CrossRef](#)]
41. Zhang, Y.; Zuo, T.T.; Cheng, Y.Q.; Lia, P.K. High-entropy alloys with high saturation magnetization, electrical resistivity and malleability. *Sci. Rep.* **2013**, *3*, 1455. [[CrossRef](#)] [[PubMed](#)]
42. Shim, S.H.; Pouraliakbar, H.; Minouei, H.; Rizi, M.S.; Fallah, V.; Na, Y.S.; Han, J.H.; Hong, S.I. Characterization of the microscale/nanoscale hierarchical microstructure of an as-cast CrMnFeNiCu high-entropy alloy with promising mechanical properties. *J. Alloys Compd.* **2023**, *954*, 170091. [[CrossRef](#)]
43. Gao, P.H.; Chen, B.Y.; Zhang, B.; Yang, Z.; Guo, Y.C.; Li, J.P.; Liang, M.X.; Li, Q.P. Preparations of iron-based alloy coatings on grey cast iron through plasma transfer arc welding. *J. Adhes. Sci. Technol.* **2022**, *36*, 833–844. [[CrossRef](#)]

Disclaimer/Publisher’s Note: The statements, opinions and data contained in all publications are solely those of the individual author(s) and contributor(s) and not of MDPI and/or the editor(s). MDPI and/or the editor(s) disclaim responsibility for any injury to people or property resulting from any ideas, methods, instructions or products referred to in the content.